

Nano-scale simulation based study of creep behavior of bimodal nanocrystalline face centered cubic metal

Md. Meraj¹ · Snehanshu Pal¹

Received: 6 July 2017 / Accepted: 24 September 2017 / Published online: 11 October 2017
© Springer-Verlag GmbH Germany 2017

Abstract In this paper, the creep behavior of nanocrystalline Ni having bimodal grain structure is investigated using molecular dynamics simulation. Analysis of structural evolution during the creep process has also been performed. It is observed that an increase in size of coarse grain causes improvement in creep properties of bimodal nanocrystalline Ni. Influence of bimodality (i.e., size difference between coarse and fine grains) on creep properties are found to be reduced with increasing creep temperature. The dislocation density is observed to decrease exponentially with progress of creep deformation. Grain boundary diffusion controlled creep mechanism is found to be dominant at the primary creep region and the initial part of the secondary creep region. After that shear diffusion transformation mechanism is found to be significantly responsible for deformation as bimodal nanocrystalline Ni transforms to amorphous structure with further progress of the creep process. The presence of $\langle 0, 2, 8, 5 \rangle$, $\langle 0, 2, 8, 2 \rangle$, and $\langle 0, 1, 10, 2 \rangle$ distorted icosahedra has a significant influence on creep rate in the tertiary creep regime according to Voronoi cluster analysis.

Keywords Molecular dynamics · Creep · Diffusion · Bimodal grain structure · Dislocation

Introduction

Nanocrystalline (NC) metals have extremely high strength but low ductility restricts their applicability [1–7]. Introduction of a bimodal grain structure in such nanocrystalline materials is capable of enhancing strength as well as ductility [8–13]. In the case of bimodal grain structure, fine nano grains (NG) impart high strength, whereas coarse grains (CG) bestow better ductility [14]. NC Ni having bimodal grain structure shows prominent strain hardening under deformation conditions as per experimental studies reported in literature [12, 15–17]. Observed high uniaxial tensile strength of polycrystalline face centered cubic (FCC) metal with bimodal grain size distribution is due to lattice dislocation activities occurring in the larger grain region according to a molecular dynamics (MD) simulation based study performed by Zhang et al. [10]. Thorough understanding of time-dependent plasticity of NC metal is necessary for improving reliability during service condition as well as estimating working life according to the engineering viewpoint. Creep behavior of free-standing FCC films having bimodal grain size (i.e., 40 and 220 nm) distribution is studied experimentally at room temperature and it is reported that the dislocation activities have significant influence on creep rate [13]. During the creep process ultrafine grained NC metal becomes amorphous as per the finding reported in literature [18–20]. It is known that shear transformation zones (STZs), shear diffusion transformation (SDT), and free volume mechanism have significant influence on creep deformation process of amorphous materials [21–24], but understanding of the creep deformation mechanism of amorphous structure at nano-scale is still far from conclusion. However, some investigations on creep behavior of NC FCC metals and alloys having grains of equal size using molecular dynamics simulation have been reported in literature [18–20, 25–28], atomistic simulation study of the influence of bimodal

✉ Snehanshu Pal
pals@nitrrkl.ac.in; snehanshu.pal@gmail.com

¹ Department of Metallurgical and Materials Engineering, National Institute of Technology Rourkela, Rourkela, Odisha 769008, India

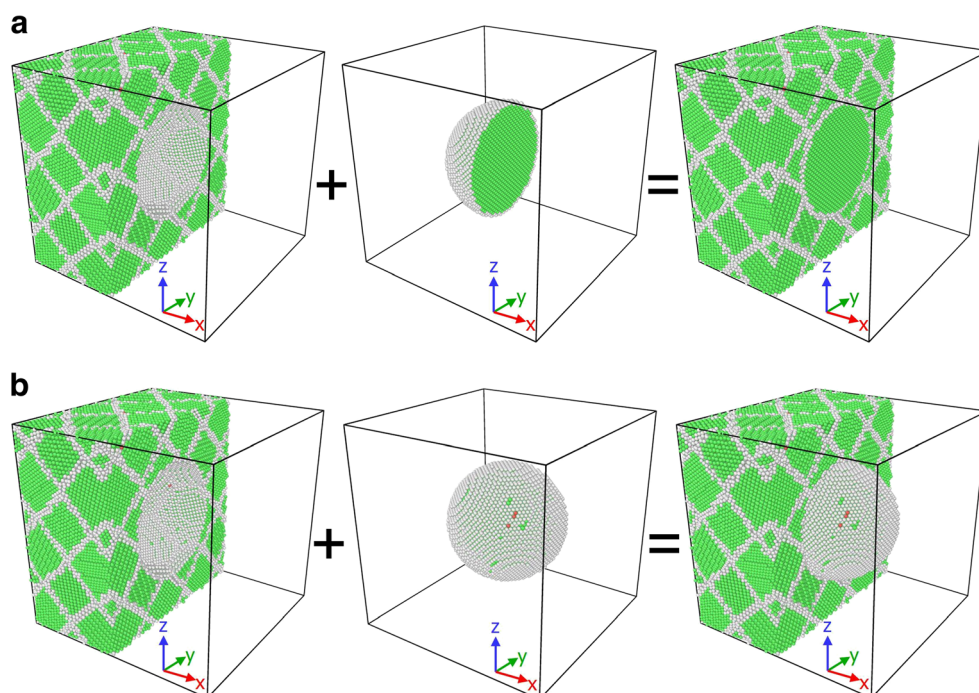
grain size distribution on creep behavior of NC metals has not been studied so far. In this paper, for the first time, we are going to discuss the creep deformation of bimodal structured nanocrystalline metal using molecular dynamics simulation along with the effect of size of bigger grain on the creep deformation process of bimodal NC Ni. Furthermore, special attention to the underlying deformation mechanism responsible for the creep process for transformed amorphous structure from bimodal NC Ni will also be given here.

Simulation details

A cubic NC Ni with an average grain size of 4 nm having 54 number of grain is constructed by Voronoi tessellation method [29] using Atomeye software [30]. After that, a sphere of the certain diameter d is deleted from the center of this cubic specimen. Finally a spherical insertion of the same diameter constructed from single crystalline Ni is placed inside the empty region to obtain the bimodal grain structure. The three bimodal specimens having 6 nm, 8 nm, and 10 nm spherical larger grains along with 4 nm small grains contain 253,220, 253,072, and 252,911 atoms respectively in a cubic simulation box of $14 \times 14 \times 14 \text{ nm}^3$ dimension. Energy minimizations or relaxations of bimodal NC Ni specimen at 900 K ($0.52 \cdot T_m$), 1300 K ($0.75 \cdot T_m$), and 1600 K ($0.93 \cdot T_m$) temperatures have been performed by using conjugate gradient method (where T_m is the melting temperature of pure Ni (i.e., $\sim 1728 \text{ K}$)). The constant-temperature, constant-volume (NVT) ensemble is used to regulate temperature by Nose-Hoover method

thermostat [31, 32]. Creep deformation process is also carried out at constant temperatures taking NVT ensemble and using Nosé-Hoover thermostat algorithm to control the temperature. Then, uniaxial tensile loading is applied initially along Y-direction [0 1 0] to reach 1 GPa load. Subsequently, deformation of specimen is allowed under constant uniaxial tensile load (1 GPa) using Berendsen barostat method [33] only along the Y-direction [0 1 0]. No load is applied in the other two directions (X and Z). Periodic boundary conditions are applied in all the direction during deformation simulation. In the periodic boundary condition, particles can be interacted across the boundary and it can also exit one end to re-enter the other end of the simulation box. The boundaries in x and z directions are also free to move. A time step of this simulation work is taken as 2 fs. The sectional view of NC Ni with a bimodal grain size distribution is shown in Fig. 1a,b. In this figure, a spherical shape of large grain having 8 nm is embedded inside a matrix of small grains of NC Ni specimen and colored according to Common neighbor analysis [34–36]. All the MD simulations work is performed using LAMMPS [37] with embedded atom method potential (EAM), which is established by Mendeleev [38]. Visualization and representation of atomic snapshots of NC Ni with a bimodal grain size distribution are done using OVITO open source software [39]. Dislocation extraction algorithm (DXA) inbuilt in OVITO [40, 41] is used to obtain the dislocation distributions of the bimodal NC Ni specimen. Dislocation density [42] is taken as the sum of all dislocation length per unit volume of the specimen. Characteristic structure evaluation during the creep deformation process has been investigated through determining

Fig. 1 Three dimensional cross-sectional view of bimodal NC Ni specimen showing (a) half and (b) full of bigger grain for better representation (colored according to common neighbor analysis (CNA))



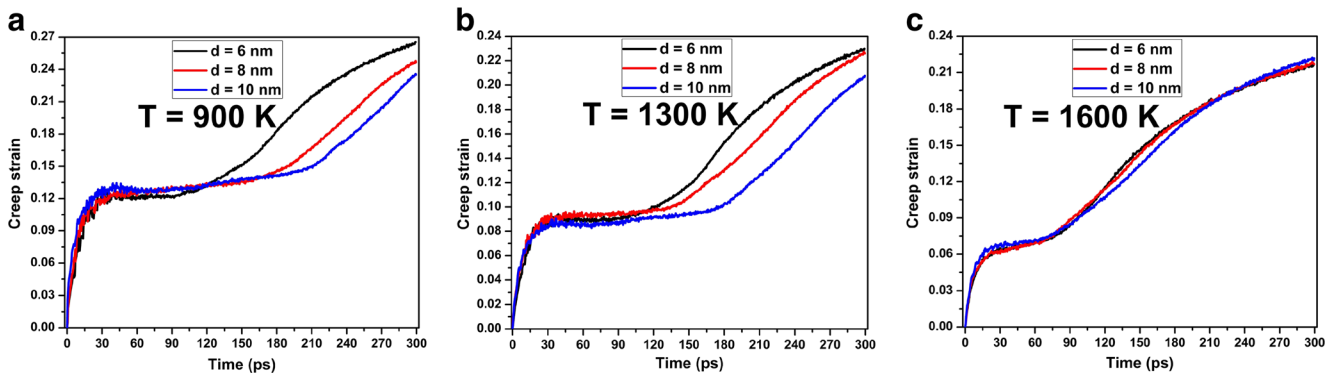


Fig. 2 Simulated creep curves of bimodal NC Ni for (a) $T = 900$ K, (b) $T = 1300$ K, and (c) $T = 1600$ K creep temperatures

population fraction of full icosahedra and distorted icosahedra in terms of Voronoi Polyhedra [19, 20]. The central symmetry parameter (CSP) is used to distinguish the degree of inversion symmetry broken as compare to each atom’s local environment of specimen under the creep deformation process [43]. CSP has zero value for perfect inversion symmetry material and nonzero value for inversion symmetry is broken during plastically deformed material. CSP for each atom is defined as follows:

$$CSP = \sum_{i=1}^{N/2} |R_i + R_{i+N/2}|^2 \tag{1}$$

where N is the number of nearest neighbors (e.g., $N = 12$, for the FCC lattice), R_i and $R_{i+N/2}$ are the vectors or bonds from the central atom to the six pairs of opposite nearest neighbors in the FCC lattice. The number of possible neighbor pairs (i, j) is given by $N(N-1)/2$ and j is equal to $i + N/2$ [43]. Each “equal and opposite” pair of bond vectors is added together, then the sum of two square bond vectors (i.e., $|R_i + R_j|^2$) is calculated. This calculation is carried out for smallest $N/2$ to evaluate CSP. R_i is generated by finding those neighbors in the distorted lattice with vectors closest in distance to the undistorted nearest-neighbor vectors. $i (1, 2, \dots, N)$ is used for defining the degree of inversion symmetry broken in each atom’s local environment.

Evaluated free volume fraction (FVF) is defined as:

$$FVF = \frac{V_{final} - V_{initial}}{V_{final}} \tag{2}$$

where $V_{initial}$ is the volume of bimodal NC Ni specimen at zero time step of creep, V_{final} is the volume of bimodal NC Ni specimen at different time steps of the creep process.

The calculation of the mean square displacement (MSD) with respect to time function equation is given below [44]:

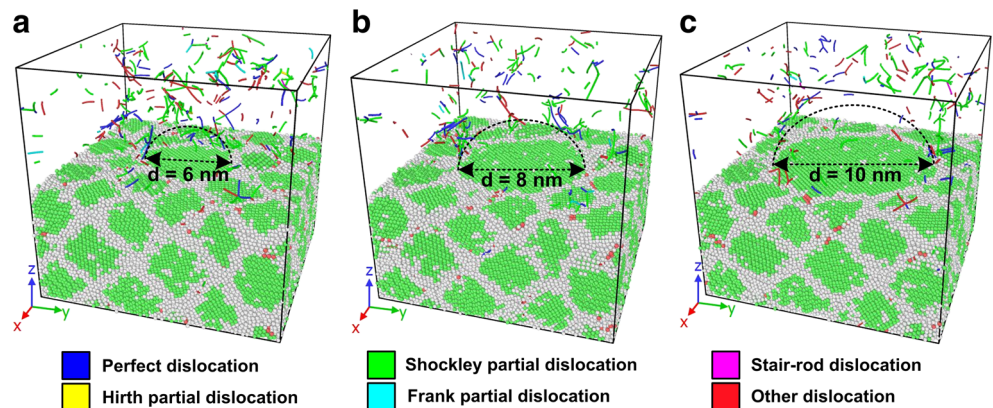
$$MSD = \langle r^2(t) \rangle = \left(\frac{1}{N} \sum_{i=0}^N (r_i(t) - r_i(0))^2 \right) \tag{3}$$

where N is the total particle number in the system, t is the time period, $r_i(t)$ is the atomic position at time t and $r_i(0)$ is the initial position of atom at time zero.

Self-diffusion coefficient (D) has been calculated using following Einstein relation [45–47]:

$$D = \frac{1}{6} \lim_{t \rightarrow \infty} \frac{MSD(t)}{t} \tag{4}$$

Fig. 3 Dislocation distribution snapshots of bimodal NC Ni having (a) $d = 6$ nm, (b) $d = 8$ nm, and (c) $d = 10$ nm bigger grains after 3 ps during creep deformation occurring at 900 K



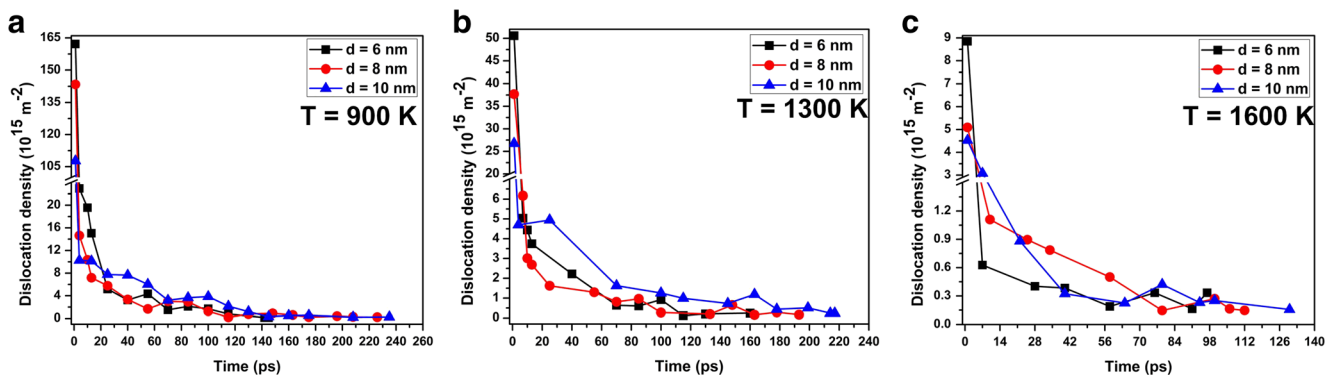


Fig. 4 Plots of evaluated dislocation density vs. time for three different larger grain sizes of bimodal NC Ni at (a) $T = 900$ K, (b) $T = 1300$ K, and (c) $T = 1600$ K creep temperatures

Results and discussion

Simulated creep curves for three bimodal NC Ni specimens having bigger grains of different size (e.g., ~ 6 , 8, and 10 nm) for 900 K, 1300 K, and 1600 K creep temperatures are presented in Fig. 2a-c to investigate the influence of size of bigger grain on creep curves of bimodal NC Ni. It is observed from Fig. 2a and b that secondary creep regime for bimodal NC Ni specimen are widened with the increase of size of bigger grain for 900 K and 1300 K creep temperatures. Creep curves for bimodal NC Ni having larger coarse grain are found to be

shifted toward lower strain in the tertiary creep regime for 900 K and 1300 K creep temperature cases (refer Fig. 2a and b). So it can be inferred that creep resistance is increased with increase of bigger grain size significantly for bimodal NC Ni specimens for moderate creep temperatures. On the other hand, creep curves of bimodal NC Ni are not found to be influenced by variation of size of bigger grains ranging from 6 to 10 nm during creep deformation occurring at 1600 K (refer Fig. 2c). This is because faster diffusion at such high creep temperature takes place and consequently quick amorphization of the entire specimen occurs. Negative creep

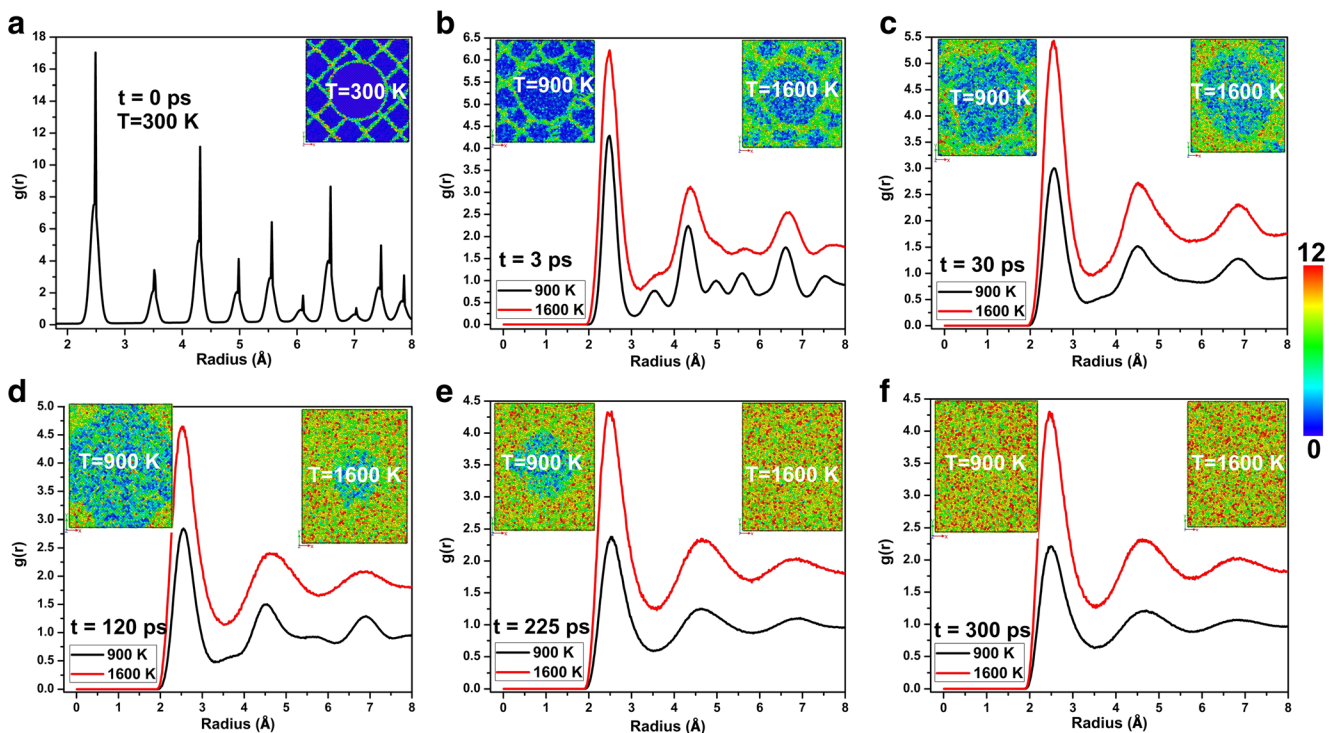
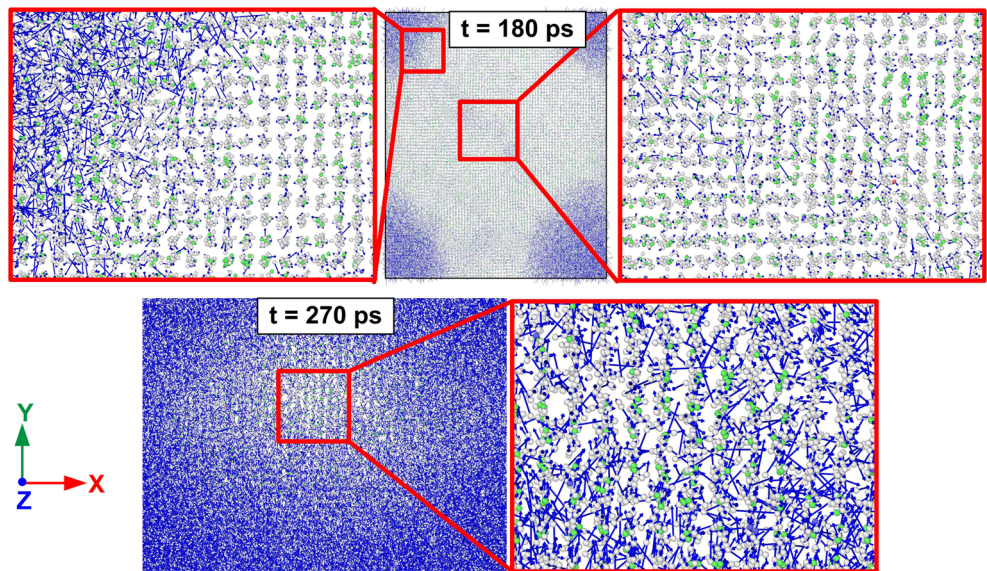


Fig. 5 Radial distribution function plots with atomic snapshots of NC Ni specimen having 8 nm coarser grain colored as per Centro-symmetry parameter at (a) initial stage and after (b) 3 ps, (c) 30 ps, (d) 120 ps, (e) 225 ps, and (f) 300 ps time periods during creep deformation occurring at 900 and 1600 K

Fig. 6 Vector plots of atomic displacements for bimodal NC Ni specimen having 10 nm of larger grain size during the creep process at 900 K after 180 ps and 270 ps time step



phenomenon is also observed at a later stage (in the tertiary creep regime) of the creep deformation process taking place at 1600 K. Negative creep normally takes place when internal stress of materials become higher than applied external stress as it causes a decrease in creep rate [20, 48]. Secondary creep regime is found to be reduced with the increase of creep temperatures (refer to Fig. 2a-c) as the diffusion process is faster at higher temperature, which in turn accelerates the creep process.

Atomic snapshots showing dislocation distribution for bimodal NC Ni having a larger grain of three different sizes after 3 ps during creep deformation occurring at 900 K are represented in Fig. 3a-c. The different types of dislocations, such as Perfect dislocation (blue), Shockley partial dislocation (green), Stair-rod dislocation (pink), Hirth partial dislocation (yellow), Frank partial dislocation (cyan), and other dislocation (red) are observed in all three specimens. According to the Burgers vector family, different types of dislocations are defined [49–51], such as $1/2 \langle 110 \rangle$ for Perfect dislocation, $1/6 \langle 112 \rangle$ for Shockley partial dislocation, $1/6 \langle 110 \rangle$ for Stair-rod dislocation, $1/3 \langle 001 \rangle$ for Hirth partial dislocation, and $1/3 \langle 111 \rangle$ for Frank partial dislocation. It is observed from Fig. 3 that the dislocations are found to be more in the region of smaller grain as compared to the region of larger grain for all the cases of bimodal NC Ni during the creep process. Consequently, at the initial stage of the creep process, the smaller grain favors deformation, while coarse grain provides better creep resistance. The evaluated dislocation density plots for bimodal NC Ni during the simulated creep process at three different temperatures (i.e., 900, 1300, and 1600 K) have been presented in Fig. 4a-c. Dislocations are found to be present a longer period in the bimodal NC Ni having larger grain during the creep deformation process. It is because formation of the amorphous structure is delayed by the presence of larger coarse grain in bimodal NC matrix. It is also observed that dislocation density is present a much longer period and higher quantity at lower creep temperature (i.e., 900 K) as compared to higher creep temperature (i.e., 1600 K). The dislocation

$1/6 \langle 112 \rangle$ for Shockley partial dislocation, $1/6 \langle 110 \rangle$ for Stair-rod dislocation, $1/3 \langle 001 \rangle$ for Hirth partial dislocation, and $1/3 \langle 111 \rangle$ for Frank partial dislocation. It is observed from Fig. 3 that the dislocations are found to be more in the region of smaller grain as compared to the region of larger grain for all the cases of bimodal NC Ni during the creep process. Consequently, at the initial stage of the creep process, the smaller grain favors deformation, while coarse grain provides better creep resistance. The evaluated dislocation density plots for bimodal NC Ni during the simulated creep process at three different temperatures (i.e., 900, 1300, and 1600 K) have been presented in Fig. 4a-c. Dislocations are found to be present a longer period in the bimodal NC Ni having larger grain during the creep deformation process. It is because formation of the amorphous structure is delayed by the presence of larger coarse grain in bimodal NC matrix. It is also observed that dislocation density is present a much longer period and higher quantity at lower creep temperature (i.e., 900 K) as compared to higher creep temperature (i.e., 1600 K). The dislocation

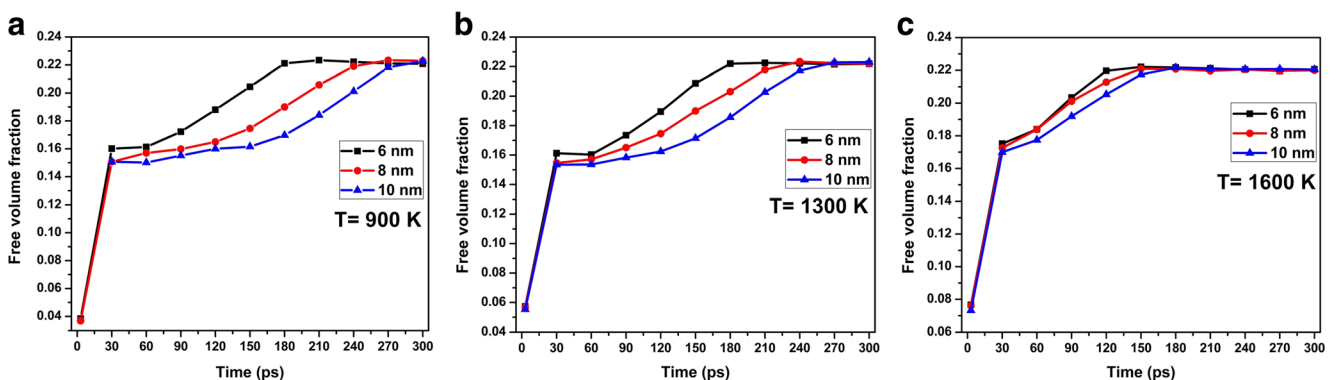


Fig. 7 Plots of evaluated free volume fraction vs. time of three different bigger grain sizes of bimodal NC Ni for (a) T = 900 K, (b) T = 1300 K, and (c) T = 1600 K creep temperatures during the creep process

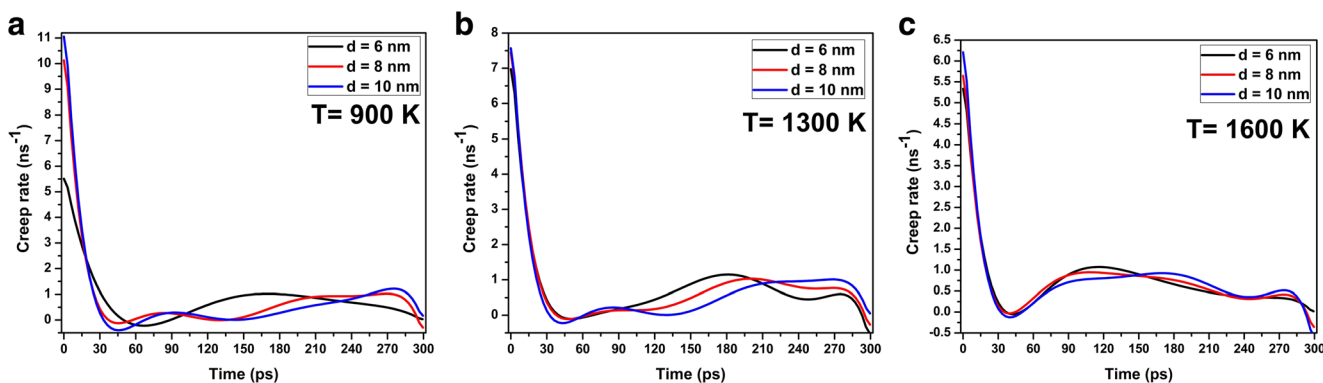


Fig. 8 Creep rate vs. time plots for three different larger grain sizes of bimodal NC Ni at (a) $T = 900$ K, (b) $T = 1300$ K, and (c) $T = 1600$ K

density of this bimodal structure is found to be decreased exponentially during the creep process for all the cases studied here, as each specimen is transformed to amorphous structure due to diffusion and accumulation of atoms in grain boundary.

Sectional view of atomic snapshots colored as per CSP along with the corresponding radial distribution function (RDF) of bimodal NC Ni specimen having 8 nm of larger grain size during the creep process for 900 K and 1600 K creep temperatures are presented in Fig. 5 as representative examples. It is observed that the grain boundary diffusion mechanism is more dominant in the region having smaller grains (i.e. ~ 4 nm) compared to the larger grain region. This actually causes initiation of amorphous structure formation in the region of smaller grains and, afterward the amorphization process moves toward the interior of larger grain from the grain boundaries between coarser grain and smaller grain with the progress of creep deformation. In another perspective, with respect to creep temperatures, amorphous structure formation is initiated earlier in the case of 1600 K compared to 900 K. It is observed that the specimen loses crystallinity with the progress of creep deformation and becomes completely amorphous after 120 ps for 1600 K and 225 ps for 900 K, as evident from Fig. 5d and e respectively. It may be due to the fact that grain boundary diffusion is faster in the case of higher

creep temperature. It is also observed that coarser grain is further increased in size at the cost of finer grain initially up to 30 ps time for 1600 K, 120 ps time for 900 K. After that, amorphization causes reduction of grain size of bigger grain, as evident from Fig. 5c and d. Moreover, first peak height (or intensity) of RDF plots for bimodal NC Ni specimen is found to be increased with increase of creep temperature, as evident from Fig. 5. This is due to the fact that larger grain is further increased in size initially at higher creep temperature as compared to lower creep temperature and consequently overall volume fraction of crystalline structure is enhanced at the initial period in the case of higher creep temperature. Vector plots of atomic displacements for bimodal NC Ni specimen having 10 nm of larger grain size during the creep process at 900 K after 180 ps and 270 ps time step are represented in Fig. 6. Atomic diffusion is found to occur from grain boundaries to the interior of bigger grain for bimodal NC specimen and randomizes the atomic arrangement inside the bigger grain as creep deformation progresses.

The evaluated free volume fraction (also called active volume) vs. time plots for bimodal NC Ni during the creep process at three different temperatures (i.e., 900, 1300, and 1600 K) are presented in Fig. 7a-c. The free volume concept has been introduced and effectively utilized for simulating the

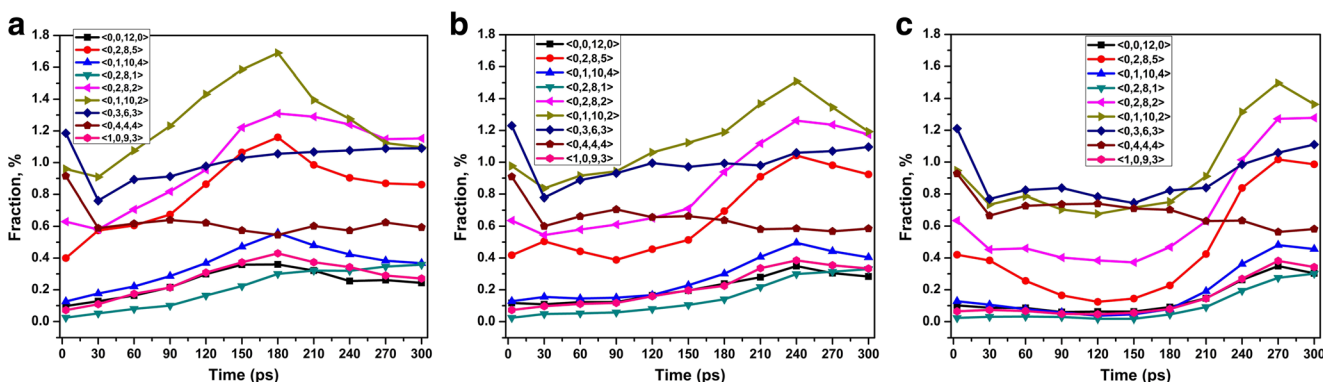


Fig. 9 Population fraction of Voronoi polyhedra vs. time plots for (a) $d = 6$ nm, (b) $d = 8$ nm, and (c) $d = 10$ nm bigger grain sizes of bimodal NC Ni at $T = 900$ K creep temperatures during the creep process

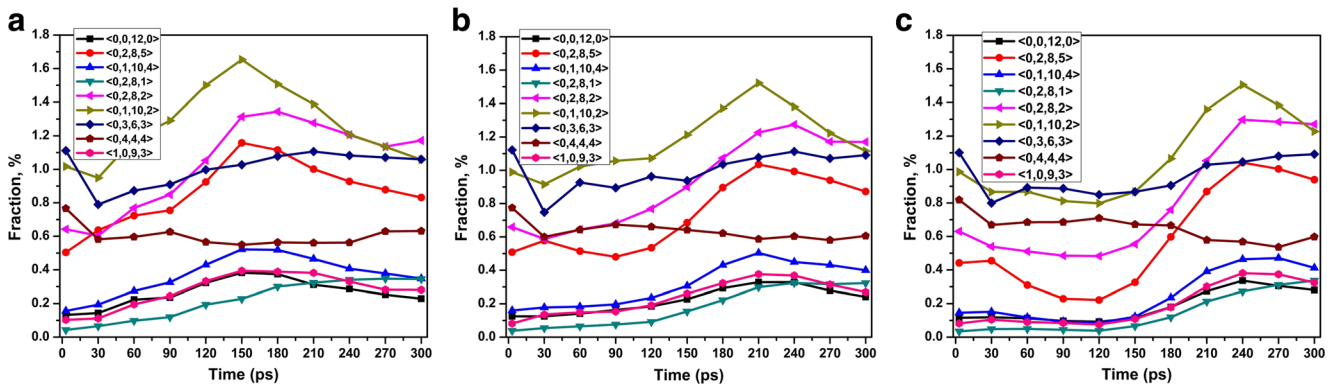


Fig. 10 Population fraction of Voronoi polyhedra vs. time plots for (a) $d = 6$ nm, (b) $d = 8$ nm, and (c) $d = 10$ nm bigger grain sizes of bimodal NC Ni at $T = 1300$ K creep temperatures during the creep process

diffusion and deformation process of metallic glass subjected to external load by Spaepen [52]. In this study from Fig. 7, free volume fraction is observed to increase very sharply at the initial stage, after that increment rate slows down, and then almost becomes constant with the progress of the creep process. It is also observed that free volume fraction curves are found to be shifted downward with increasing the size of bigger grain present in bimodal NC Ni specimen but at 300 ps, all curves converge to the same point (refer Fig. 7). Critical investigation of creep curve plots (refer Fig 2a-c) and corresponding active volume plots (refer Fig. 7) shows that change in active volume has significant influence on creep behavior. This may be due to the fact that generated active volume during deformation process can cause strain softening and strain localization [53]. Creep rate vs. time curves for bimodal NC Ni specimens having three different bigger grains size at 900 K, 1300 K, and 1600 K creep temperatures are presented in Fig. 8a-c. It is observed from Fig. 8a and b that the creep rate of secondary creep regime for 900 K and 1300 K creep temperatures becomes slower as the size of the bigger grain of bimodal NC specimen increases. Voronoi analysis is performed to study the polyhedra environment during the creep deformation process for bimodal NC Ni specimens

and the variation of population fraction of Voronoi polyhedra during the creep process occurring at 900 K, 1300 K, and 1600 K have been presented in Figs. 9, 10, and 11 respectively. Variation in population of full icosahedra (i.e., $\langle 0, 0, 12, 0 \rangle$) is very minimum and almost negligible compared to that of distorted icosahedra. Population of distorted icosahedra having voronoi indices $\langle 0, 2, 8, 5 \rangle$, $\langle 0, 2, 8, 2 \rangle$, and $\langle 0, 1, 10, 2 \rangle$ are found to reach maximum value around 150 ps to 180 ps (refer Fig. 9a), 210 ps to 270 ps (refer to Fig. 9b), and 270 ps (refer to Fig. 9c) time periods for different bimodal NC Ni specimens having 6 nm, 8 nm, and 10 nm coarse grain respectively. Interestingly, after secondary creep regime creep rate increases to its maximum value in the above mentioned time range for respective bimodal NC specimens for the creep process occurring at 900 K (refer to Fig. 8a). Similar correspondence are seen between creep rate vs time plots (refer to Fig. 8b and c) and variation in population of distorted icosahedra (refer to Figs. 10 and 11) during the creep process taking place at 1300 K and 1600 K. At this juncture, it can be inferred that the presence of $\langle 0, 2, 8, 5 \rangle$, $\langle 0, 2, 8, 2 \rangle$, and $\langle 0, 1, 10, 2 \rangle$ Voronoi polyhedra has a significant influence on creep behavior in the tertiary creep regime. In the case of creep process occurring at 1600 K, the population of Voronoi

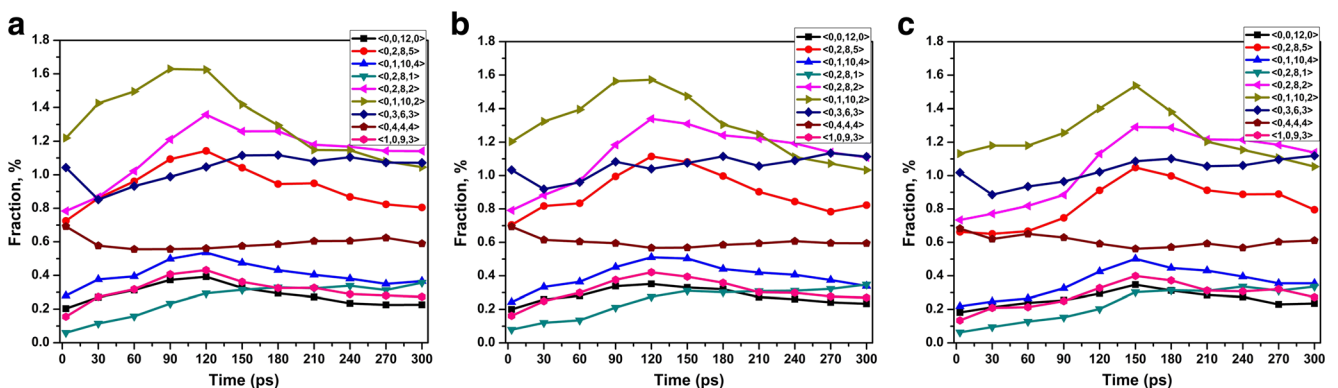


Fig. 11 Population fraction of Voronoi polyhedra vs. time plots for (a) $d = 6$ nm, (b) $d = 8$ nm, and (c) $d = 10$ nm bigger grain sizes of bimodal NC Ni at $T = 1600$ K creep temperatures during the creep process

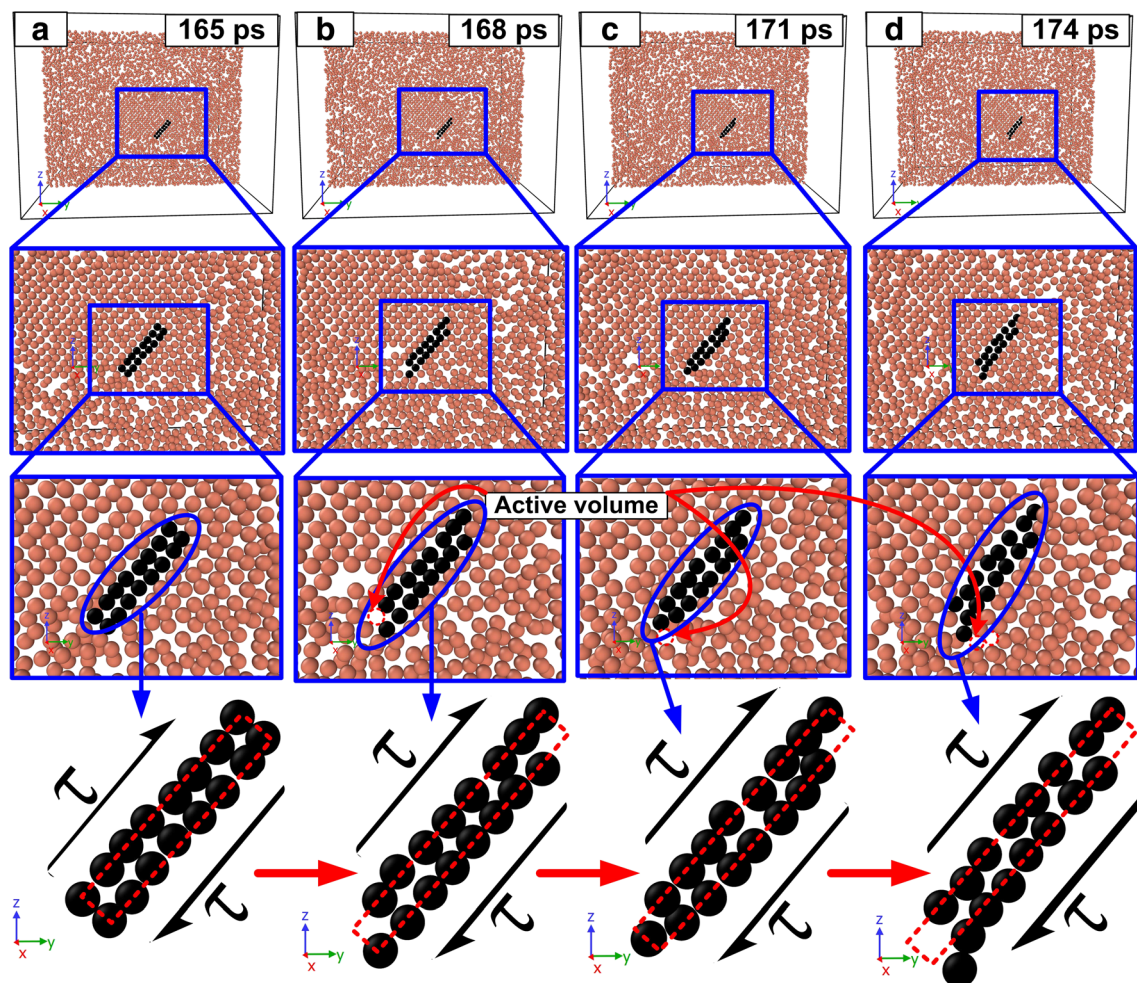


Fig. 12 Atomic snapshots indicating shear diffusion transformation (SDT) in transient creep regime

polyhedra vs. creep time plots are found to exhibit the same trend for all three specimens (refer to Fig. 11) and the deviation in the nature of creep curve of all three bimodal NC specimens is negligible for such high creep temperature (refer to Fig. 2c) as well. To sum up, variation in distorted Voronoi polyhedra population is an

influencing factor for the creep process of such bimodal NC specimens when it converts to amorphous structure. This can be accounted for by the fact that the structures with a lower degree of local fivefold symmetry (LFFS), such as $\langle 0, 2, 8, 5 \rangle$, $\langle 0, 2, 8, 2 \rangle$, and $\langle 0, 1, 10, 2 \rangle$ clusters are capable of accommodating larger plastic

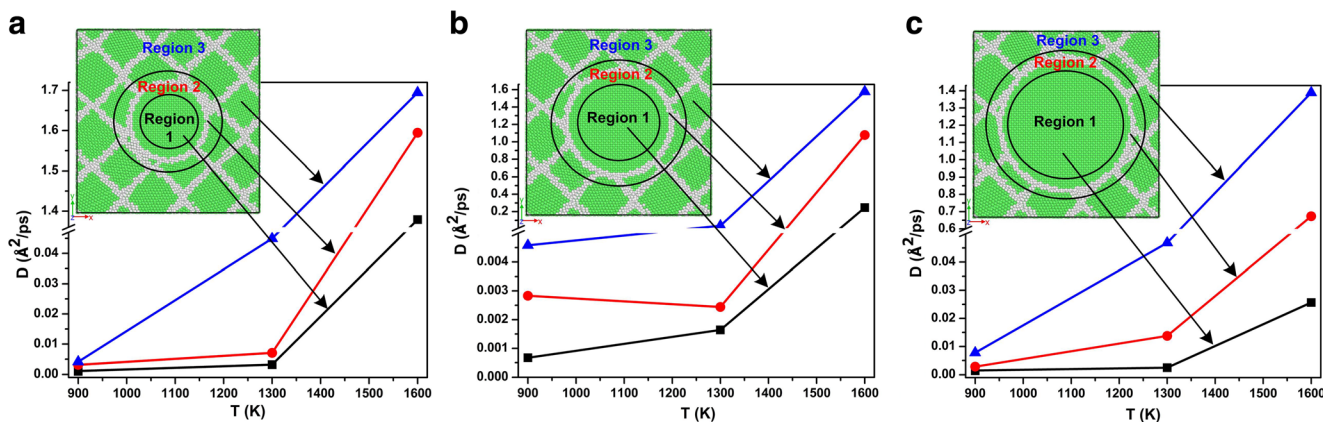


Fig. 13 Self-diffusion coefficient (D) plots of bimodal NC Ni at three different regions with respect to temperature for (a) $d = 6$ nm, (b) $d = 8$ nm, and (c) $d = 10$ nm bigger grains

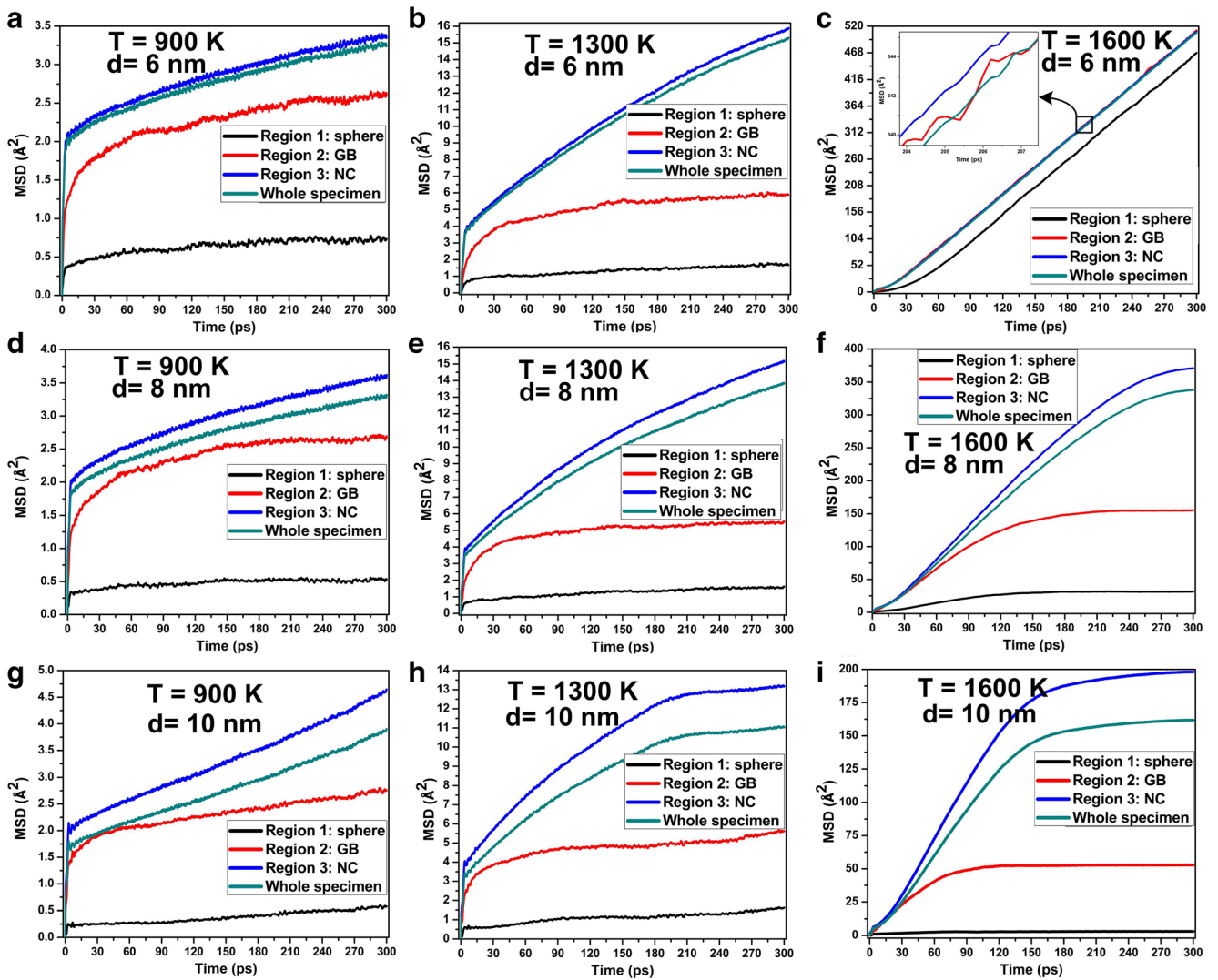


Fig. 14 Mean square displacement (MSD) vs. time plots for different temperatures and different larger grain sizes of bimodal NC Ni at three different regions and whole specimen

deformation in the case of metallic glass [53, 54]. Actually, the lower degree of LFFS such as $\langle 0, 2, 8, 5 \rangle$, $\langle 0, 2, 8, 2 \rangle$, and $\langle 0, 1, 10, 2 \rangle$ clusters increases

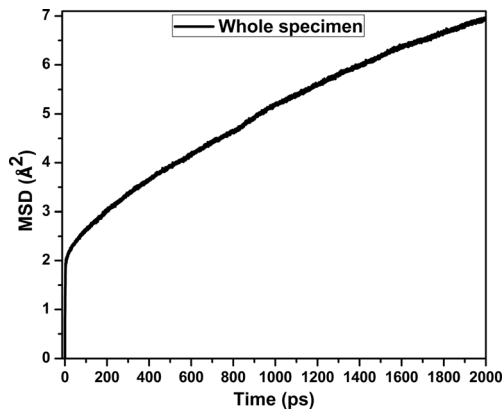
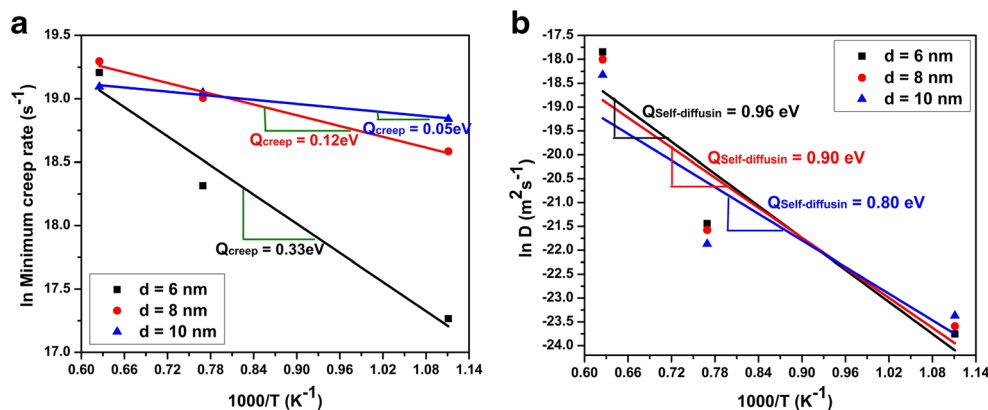


Fig. 15 MSD vs. time plot for whole bimodal NC Ni specimen having 6 nm larger grain size (calculated at 900 K)

the defects and favors plastic deformation in comparison with the $\langle 0, 0, 12, 0 \rangle$ full icosahedra [53].

Atomic configurational snapshots of bimodal NC Ni having 6 nm bigger grain size after 165 ps, 168 ps, 171 ps, and 174 ps time steps indicating shear diffusion transformation (SDT) during creep deformation process at 900 K are represented in Fig. 12a-d. SDT is found to start at the initial stage of tertiary creep regime for bimodal NC Ni having 6 nm bigger grain size specimen at 900 K creep temperature and the amorphization of bimodal NC Ni specimen is also intensified at that time. It is observed that stress-driven shear diffusion transformation (SDT) mechanism is operative when bimodal NC Ni specimens become amorphous; it is also found in previously reported literature that SDT is responsible for deformation of amorphous materials [24, 55, 56]. It is observed from Fig. 12 that SDT also helps to create active volume during creep deformation process.

Fig. 16 (a) logarithmic of minimum creep rate vs $1000/\text{temperature}(\text{K})$ for a constant 1 GPa applied load, (b) logarithmic of D for whole specimen of bimodal NC Ni vs. $1000/\text{temperature}$



Self-diffusion (D) vs temperature (T) plots of three different regions for bimodal NC Ni having 6, 8, and 10 nm of larger grains are presented in Fig. 13a-c, which are calculated from the slope of the mean square displacement (MSD) curves only in the linear region obtained for different temperature as shown in Fig. 14. A representative MSD simulation was carried out for bimodal NC Ni having 6 nm larger grain at 900 K for 2000 ps time period and corresponding MSD vs. time plot is presented in Fig. 15. The value of calculated diffusion coefficient for this representative case is almost the same for the MSD calculation performed for the 300 ps and 2000 ps time period as the slope of linear region of MSD curve is not varied in the MSD calculation time period from 300 ps to 2000 ps (evident from Fig. 15). Self-diffusion of atoms in an MD simulation is determined via the Einstein relations, which include tracking atomic displacements or velocities of atoms [57, 58]. Inner portion of larger grain is designated as region 1 and grain boundary between the larger grain and smaller grain is considered as region 2 whereas region 3 indicates the region having smaller grains. It is observed that self-diffusion in these three different regions of specimen are increased as temperature increases. It is observed from Fig. 13a-c that maximum self-diffusion happens in the region with smaller grains (i.e., region 3), while minimum occurs in the inner part of the larger grain (i.e., region 1) for bimodal NC Ni specimens. Moreover, self-diffusion plots for bimodal NC Ni specimen is shifted upward from region 1 (i.e., large grain) to region 3 (i.e., smaller grain) with increasing temperature, as evident from Fig. 13a-c. Activation energies of creep and diffusion processes for bimodal NC Ni specimen are calculated from the slope of the \ln minimum creep rates and diffusivities versus $1/T$ curves as shown in Fig. 16a and b. Obtained activation energies for creep of bimodal NC Ni having coarser gains of 6 nm, 8 nm, and 10 nm sizes are equal to 0.33 eV, 0.12 eV, and 0.05 eV respectively, while activation energies for self-diffusion of bimodal NC Ni having 6 nm, 8 nm, and 10 nm is equal to 0.96 eV, 0.90 eV, and 0.80 eV respectively. In this investigation, activation energy of creep for bimodal NC Ni having 6 nm, 8 nm, and 10 nm large grains is found to be less

compared to the activation energy of self-diffusion for the same system. This difference can be attributed to the fact that activation energy for the creep process is calculated when external load is applied on the specimen, whereas activation energy for the self-diffusion process is obtained without any external applied load. It is also observed that activation energies of bimodal NC Ni are decreased with the increase in size of larger grains for both the creep process and self-diffusion process.

Conclusions

In summary, it can be inferred that creep property of bimodal NC Ni specimens is enhanced with the increase in size of larger grain. Maximum self-diffusion happens in the smaller grains region, while minimum self-diffusion occurs in the larger grain region of bimodal NC Ni specimens. The Coble creep mechanism is significantly dominant for NC Ni having bimodal grain distribution during nanocrystalline phase, while the shear diffusion transformation mechanism is operative after bimodal NC Ni transforms to amorphous structure. Free volume fraction curves for bimodal NC Ni are observed to be shifted downward with increasing the size of bigger grain during the creep process but converged after 300 ps. Dislocations for bimodal NC Ni are found to be present for a longer period with increasing size of the bigger grain during the creep process.

References

1. Beyerlein IJ, Demkowicz MJ, Misra A, Uberuaga BP (2015) Defect-interface interactions. *Prog Mater Sci* 74:125–210
2. Khan AS, Liu J (2016) A deformation mechanism based crystal plasticity model of ultrafine-grained/nanocrystalline FCC polycrystals. *Int J Plast* 86:56–69

3. Wu CD, Tsai HW (2017) Atomistic simulation study of tensile deformation in nanocrystalline and single-crystal Au. *J Mol Model* 23:114-1-6
4. Rodríguez-Galán D, Sabirov I, Segurado J (2015) Temperature and strain rate effect on the deformation of nanostructured pure titanium. *Int J Plast* 70:191-205
5. Rupert TJ (2016) The role of complexions in metallic nano-grain stability and deformation. *Curr Opin Solid State Mater Sci* 20:257-267
6. Choi Y, Park Y, Hyun S (2012) Mechanical properties of nanocrystalline copper under thermal load. *Phys Lett A* 376:758-762
7. Li J, Weng GJ, Chen S, Wu X (2017) On strain hardening mechanism in gradient nanostructures. *Int J Plast* 88:89-107
8. Zhu L, Lu J (2012) Modelling the plastic deformation of nanostructured metals with bimodal grain size distribution. *Int J Plast* 30:166-184
9. Ma E (2003) Instabilities and ductility of nanocrystalline and ultrafine-grained metals. *Scr Mater* 49:663-668
10. Zhang F, Liu Z, Zhou J (2016) Molecular dynamics simulation of micro-mechanical deformations in polycrystalline copper with bimodal structures. *Mater Lett* 183:261-264
11. Wang YM, Ma E (2004) Three strategies to achieve uniform tensile deformation in a nanostructured metal. *Acta Mater* 52:1699-1709
12. Wang Y, Chen M, Zhou F, Ma E (2002) High tensile ductility in a nanostructured metal. *Nature* 419:912-915
13. Guo NN, Zhang JY, Cheng PM, Liu G, Sun J (2013) Room temperature creep behavior of free-standing Cu films with bimodal grain size distribution. *Scr Mater* 68:849-852
14. Magee A, Ladani L, Topping TD, Lavernia EJ (2012) Effects of tensile test parameters on the mechanical properties of a bimodal Al-Mg alloy. *Acta Mater* 60:5838-5849
15. Zhao Y, Topping T, Bingert JF, Thornton JJ, Dangelewicz AM, Li Y, Liu W, Zhu Y, Zhou Y, Lavernia EJ (2008) High tensile ductility and strength in bulk nanostructured nickel. *Adv Mater* 20:3028-3033
16. Horita Z, Ohashi K, Fujita T, Kaneko K, Langdon TG (2005) Achieving high strength and high ductility in precipitation-hardened alloys. *Adv Mater* 17:1599-1602
17. Yip S (2003) Synergistic science. *Nat Mater* 2:3-5
18. Meraj M, Yedla N, Pal S (2016) The effect of porosity and void on creep behavior of ultra-fine grained nano crystalline nickel. *Mater Lett* 169:265-268
19. Pal S, Meraj M (2016) Structural evaluation and deformation features of interface of joint between nano-crystalline Fe-Ni-Cr alloy and nano-crystalline Ni during creep process. *Mater Des* 108:168-182
20. Pal S, Meraj M, Deng C (2017) Effect of Zr addition on creep properties of ultra-fine grained nanocrystalline Ni studied by molecular dynamics simulations. *Comput Mater Sci* 126:382-392
21. Kassner ME, Smith K, Eliasson V (2015) Creep in amorphous metals. *J Mater Res Technol* 4:100-107
22. Jiang MQ, Wilde G, Dai LH (2015) Origin of stress overshoot in amorphous solids. *Mech Mater* 81:72-83
23. Schuh CA, Hufnagel TC, Ramamurty U (2007) Mechanical behavior of amorphous alloys. *Acta Mater* 55:4067-4109
24. Mao Y, Li J, Lo YC, Qian X, Ma E (2015) Stress-driven crystallization via shear-diffusion transformations in a metallic glass at very low temperatures. *Phys Rev B* 91:214103-1-8
25. Nie K, Wu WP, Zhang XL, Yang SM (2017) Molecular dynamics study on the grain size, temperature, and stress dependence of creep behavior in nanocrystalline nickel. *J Mater Sci* 52:2180-2191
26. Darling KA, Rajagopalan M, Komarasamy M, Bhatia MA, Hornbuckle BC, Mishra RS, Solanki KN (2016) Extreme creep resistance in a microstructurally stable nanocrystalline alloy. *Nature* 537:378-381
27. Meraj M, Pal S (2017) Healing mechanism of nanocrack in nanocrystalline metals during creep process. *Appl Phys A Mater Sci Process* 123:138-1-7
28. Meraj M, Pal S (2017) Comparative creep behaviour study between single crystal Nickel and ultra-fine grained nano crystalline Nickel in presence of porosity at 1120 K temperature. *Metall Res Technol* 114:107-1-11
29. Chen D (1995) Structural modeling of nanocrystalline materials. *Comput Mater Sci* 3:327-333
30. Li J (2003) AtomEye: an efficient atomistic configuration viewer. *Model Simul Mater Sci Eng* 11:173-177
31. Nosé S (1984) A unified formulation of the constant temperature molecular dynamics methods. *J Chem Phys* 81:511-519
32. Hoover WG (1985) Canonical dynamics: equilibrium phase-space distributions. *Phys Rev A* 31:1695-1697
33. Berendsen HJ, Postma JV, van Gunsteren WF, DiNola ARHJ, Haak JR (1984) Molecular dynamics with coupling to an external bath. *J Chem Phys* 81:3684-3690
34. Jónsson H, Andersen HC (1988) Icosahedral ordering in the Lennard-Jones liquid and glass. *Phys Rev Lett* 60:2295-2298
35. Clarke AS, Jónsson H (1993) Structural changes accompanying densification of random hard-sphere packings. *Phys Rev E* 47:3975-3984
36. Stukowski A (2012) Structure identification methods for atomistic simulations of crystalline materials. *Model Simul Mater Sci Eng* 20:045021-1-15
37. Plimpton S (1995) Fast parallel algorithms for short-range molecular dynamics. *J Comput Phys* 117:1-19
38. Mendelev MI, Kramer MJ, Hao SG, Ho KM, Wang CZ (2012) Development of interatomic potentials appropriate for simulation of liquid and glass properties of NiZr2 alloy. *Philos Mag* 92:4454-4469
39. Stukowski A (2009) Visualization and analysis of atomistic simulation data with OVITO—the Open Visualization Tool. *Model Simul Mater Sci Eng* 18:015012-1-7
40. Stukowski A, Albe K (2010) Extracting dislocations and non-dislocation crystal defects from atomistic simulation data. *Model Simul Mater Sci Eng* 18:085001-1-13
41. Stukowski A, Bulatov VV, Arsenlis A (2012) Automated identification and indexing of dislocations in crystal interfaces. *Model Simul Mater Sci Eng* 20:085007-1-16
42. von Blanckenhagen B, Arzt E, Gumbsch P (2004) Discrete dislocation simulation of plastic deformation in metal thin films. *Acta Mater* 52:773-784
43. Kelchner CL, Plimpton SJ, Hamilton JC (1998) Dislocation nucleation and defect structure during surface indentation. *Phys Rev B* 58:11085-11088
44. Rose JP, Berry RS (1992) Towards elucidating the interplay of structure and dynamics in clusters: small KCl clusters as models. *J Chem Phys* 96:517-538
45. Einstein A (1905) On the motion of small particles suspended in liquids at rest required by the molecular-kinetic theory of heat. *Ann Phys* 17:549-560
46. Debela TT, Wang XD, Cao QP, Zhang DX, Wang SY, Wang CZ, Jiang JZ (2013) Atomic structure evolution during solidification of liquid niobium from ab initio molecular dynamics simulations. *J Phys Condens Matter* 26:055004-1-8
47. Razmara N, Mohammadzadeh R (2017) Molecular dynamics study of nitrogen diffusion in nanocrystalline iron. *J Mol Model* 23:8-1-6
48. Zhang JS (2010) High temperature deformation and fracture of materials. Elsevier, New Delhi
49. Stukowski A, Albe K (2010) Dislocation detection algorithm for atomistic simulations. *Model Simul Mater Sci Eng* 18:025016-1-15
50. Stukowski A (2014) Computational analysis methods in atomistic modeling of crystals. *JOM* 66:399-407

51. Maras E, Trushin O, Stukowski A, Ala-Nissila T, Jónsson H (2016) Global transition path search for dislocation formation in Ge on Si (001). *Comput Phys Commun* 205:13–21
52. Spaepen F (1977) A microscopic mechanism for steady state inhomogeneous flow in metallic glasses. *Acta Metall* 25:407–415
53. Feng S, Qi L, Wang L, Pan S, Ma M, Zhang X, Li G, Liu R (2015) Atomic structure of shear bands in Cu₆₄Zr₃₆ metallic glasses studied by molecular dynamics simulations. *Acta Mater* 95:236–243
54. Peng HL, Li MZ, Wang WH (2011) Structural signature of plastic deformation in metallic glasses. *Phys Rev Lett* 106:135503-1-4
55. Argon AS (1979) Plastic deformation in metallic glasses. *Acta Metall.* 27:47–58
56. Li W, Rieser JM, Liu AJ, Durian DJ, Li J (2015) Deformation-driven diffusion and plastic flow in amorphous granular pillars. *Phys Rev E* 91:062212-1-13
57. Frenkel D, Smit B (2002) *Understanding molecular simulation from algorithms to simulations*. Academic, San Diego
58. Sellers MS, Schultz AJ, Basaran C, Kofke DA (2011) Effect of Cu and Ag solute segregation on β Sn grain boundary diffusivity. *J Appl Phys* 110:013528-1-9